



Disparities in Magnetic Cloud Observations between Two Spacecraft Having Small Radial and Angular Separations near 1 au

Anjali Agarwal^{1,2} and Wageesh Mishra^{1,2} ¹ Indian Institute of Astrophysics, II Block, Koramangala, Bengaluru 560034, India; anjaliagarwal1024@gmail.com, m.wageesh30@gmail.com² Pondicherry University, R.V. Nagar, Kalapet 605014, Puducherry, India

Received 2025 January 17; revised 2025 February 25; accepted 2025 February 25; published 2025 March 28

Abstract

Studies for inferring the global characteristics of coronal mass ejections (CMEs) from multipoint local in situ observations have been undertaken previously, but limited studies have utilized measurements from multiple spacecraft with sufficiently small radial and angular separations. In the present study, we investigate a magnetic cloud (MC) region of a CME observed in situ during 2023 September 24–26 by the STEREO-A and Wind spacecraft near 1 au, which had radial and angular separations of 0.03 au and 3.4° , respectively. We examine the disparities in the estimates of the arrival times of CME substructures, the MC axis, and its orientation between the two spacecraft. We also propose an approach for identifying the MC axis's arrival and have compared it with the arrival of the size center and time center to understand the nonisotropic compression of the MC along its angular extent. Using minimum variance analysis, we note that the orientation of the MC is slightly out of the ecliptic at Wind but not at STEREO-A. We also compare the magnetic field parameters from the start to the end of the MC at both spacecraft and note a significant noncoherency in the MC toward its trailing portion. Our analysis confirms that the MC has a stronger compression at the rear portion at STEREO-A than at Wind, with its trailing edge arriving later at Wind. Our study highlights substantial differences in CME characteristics even at mesoscales across the angular extent, and therefore one needs to analyze several such cases to better understand the flux rope structure.

Unified Astronomy Thesaurus concepts: [Solar coronal mass ejections \(310\)](#)

1. Introduction

Coronal mass ejections (CMEs) are energetic expulsions of magnetized plasma bubbles from the Sun's corona into the heliosphere and are major sources of space weather effects (R. Schwenn 2006; T. Pulkkinen 2007; D. F. Webb & T. A. Howard 2012; C. J. Schrijver et al. 2015). CMEs are often observed using remote and in situ observations, and these two sets of observations have inherent advantages and limitations. There have been several attempts made to understand the global morphology, structures, orientation, and evolution of 3D kinematics and thermodynamics of CMEs in the heliosphere using remote and in situ observations combined with modeling (N. R. Sheeley et al. 1999; H. Xie et al. 2004; A. F. R. Themisien et al. 2006; J. A. Davies et al. 2013; W. Mishra & N. Srivastava 2015; W. Mishra & Y. Wang 2018; S. Khuntia et al. 2023; W. Mishra et al. 2023). The in situ observations of a CME have been used to clearly identify its substructures, such as shock, sheath, and a flux rope that is identified as a magnetic cloud (MC), because their plasma properties are inherently different from each other (T. H. Zurbuchen & I. G. Richardson 2006; W. Mishra & L. Teriaca 2023; M. Temmer et al. 2023). However, the possibility of identifying different substructures depends on the 1D trajectory of the in situ spacecraft through the global CME structure (L. Burlaga et al. 1981; N. U. Crooker & D. S. Intriligator 1996; V. Bothmer & R. Schwenn 1998; T. Nieves-Chinchilla et al. 2013). For example, only 30%–40% of CMEs exhibit flux rope (i.e., magnetic cloud) structure in the

in situ observations (J. T. Gosling 1990; H. Q. Song et al. 2020; W. Mishra et al. 2021b), although this does not mean that flux ropes are absent from CMEs. It is considered that the signatures of missing flux ropes in CMEs are due to the absence of a favorable trajectory of the spacecraft through the CME (N. Gopalswamy 2006; J. Zhang et al. 2013). Therefore, observations from multiple in situ spacecraft can be inconsistent in terms of detecting some substructures, and further, the in situ observations of the magnetic field and plasma parameters of the same substructures from multiple viewpoints can provide their 3D morphology and structures (E. K. J. Kilpua et al. 2011; N. Lugaz et al. 2018; W. Mishra et al. 2021a).

From the space weather perspective, the magnetic field and plasma parameters of different substructures in a CME can play an important role in deciding their consequences on the Earth (W. D. Gonzalez et al. 1999; Y. Wang et al. 2003; N. Srivastava & P. Venkatakrishnan 2004; B. E. Wood et al. 2017). Furthermore, these parameters are expected to be different at different radial distances from the Sun as CMEs evolve in the ambient solar wind during their interplanetary (IP) journey from the Sun to 1 au. Further, some studies have suggested that CME properties measured at longitudinally separated in situ spacecraft can differ, even if the multiple spacecraft are in the same plane and at the same radial distance from the Sun. This could be due to certain geometrical structures of a CME and its flux rope, noncoherent magnetic field structures inside CMEs, inhomogeneity in the background solar wind, and nonisotropic expansion of CMEs (N. Gopalswamy 2006; M. J. Owens et al. 2017; H. Cremades et al. 2020; R. T. Desai et al. 2020; C. Kay & T. Nieves-Chinchilla 2021; W. Mishra et al. 2021a). N. Lugaz et al. (2022) found that the western leg of a CME moves more slowly than its eastern leg, which results in the formation of shock at the western leg; they suggested that the local



Original content from this work may be used under the terms of the [Creative Commons Attribution 4.0 licence](#). Any further distribution of this work must maintain attribution to the author(s) and the title of the work, journal citation and DOI.

parameters of CMEs as observed by in situ spacecraft are also influenced by the surrounding ambient medium. Additionally, N. Al-Haddad & N. Lugaz (2025) have emphasized the complexity of CME substructures, their deformation in the IP medium, and the necessity of multipoint in situ observations for a better understanding and representation of CMEs. Therefore, multipoint in situ spacecraft observations are required to understand the CME parameters globally and investigate the physics of CME evolution.

In the era of Helios, the Interplanetary Monitoring Platform, Pioneer, and Voyager spacecraft, studies utilizing multipoint in situ observations have suggested that CMEs can have a greater expansion closer to the Sun and their flux ropes (i.e., MCs) can have highly distended cross sections (in the longitudinal dimension) in the IP medium with respect to the radial size of CMEs (L. Burlaga et al. 1981; N. U. Crooker & D. S. Inrligator 1996; V. Bothmer & R. Schwenn 1998). However, such studies utilized observations from in situ spacecraft that were largely separated radially as well as longitudinally from each other. Therefore, such studies could not discern the effects of a CME's temporal evolution with its inherent inhomogeneity on the plasma parameters measured at different spacecraft. This is because CME plasma parameters observed by radially aligned in situ spacecraft can differ due to their temporal evolution, while they can also differ at the longitudinally separated in situ spacecraft due to the inherent inhomogeneity in the CME and its noncoherent evolution. Moreover, these studies could be compromised in the absence of imaging observations as it would be difficult to ascertain whether the same CME substructures were sampled at the different locations of multiple in situ spacecraft.

The launch of the twin Solar Terrestrial Relations Observatory (STEREO; R. A. Howard et al. 2008; M. L. Kaiser et al. 2008) with the planetary missions MESSENGER and Venus Express provided the opportunity to analyze multipoint in situ measurements of CMEs at radially and longitudinally separated locations. Using radially aligned multipoint in situ spacecraft (with small separation in longitude), several attempts were made to study the radial/temporal evolution of the CME and to determine the power law of its radial width and the strength of the axial magnetic field with heliocentric distance (Y. Liu et al. 2005; M. Leitner et al. 2007; A. M. Gulisano et al. 2010; S. W. Good et al. 2015, 2018; N. Lugaz et al. 2020; T. M. Salman et al. 2020; E. E. Davies et al. 2021a). Additionally, utilizing the temporal evolution and kinematics of the CME in the IP medium, there are models to examine the thermodynamic properties of the CME (W. Mishra & Y. Wang 2018; W. Mishra et al. 2020; S. Khuntia et al. 2023). Moreover, utilizing the newer spacecraft Parker Solar Probe (PSP), Solar Orbiter (SolO), and BepiColombo, which are often separated by large radial distances and small/large longitudes, there are studies exploring the radial/temporal evolution of CMEs and their substructures in the background solar wind medium (E. E. Davies et al. 2021b; E. K. J. Kilpua et al. 2021; R. M. Winslow et al. 2021; C. Möstl et al. 2022; F. Regnault et al. 2023). The interaction of CMEs with other large-scale solar wind structures (e.g., heliospheric current sheet, preceding CMEs, and stream interaction regions) can also lead to changes in their properties on different spatial scales (N. Gopalswamy et al. 2009; R. M. Winslow et al. 2016; W. Mishra et al. 2017, 2021a; E. K. J. Kilpua et al. 2019; N. Lugaz et al. 2022).

It is obvious that there are only a handful of studies exploring CME characteristics measured by multiple spacecraft located at nearly the same distance from the Sun but with a small longitudinal separation (E. K. J. Kilpua et al. 2011; N. Lugaz et al. 2018). Thus, there remains a gap in exploring the CME properties at small spatial/mesoscale, which is possible if multiple spacecraft sampling the CME have mutual radial separations of 0.005–0.05 au and longitudinal separations of 1° – 12° (N. Lugaz et al. 2018). Such observations at the mesoscale can emphasize the inherent inhomogeneity of CMEs or their different substructures. It is possible that the temporal evolution of each mesoscale substructure of a CME is different, and they go through different physical processes during their IP journey. Therefore, it is necessary to conduct a comprehensive study of CME substructures observed by two or more in situ spacecraft separated by only a small spatial/longitudinal extent, which can reveal the physics of CMEs at the mesoscale.

In this paper, we focus on the difference in the magnetic field and plasma parameters of a selected CME flux rope at mesoscales measured by STEREO-A (A. B. Galvin et al. 2008; J. G. Luhmann et al. 2008) and Wind (K. W. Ogilvie & M. D. Desch 1997) because these two spacecraft provide a rare and favorable conjunction for such a study. The selected CME is found to arrive near 1 au on 2023 September 24–26, when the radial and angular separations between the two spacecraft are 0.03 au ($\sim 6.4 R_\odot$) and $\sim 3.4^\circ$, respectively, corresponding to an arc length of around 0.06 au, taking them to be at 0.99 au. We also focus on a novel approach to determine the flux rope's axis (termed the axis center), utilizing the magnetic field parameters of the flux rope (i.e., MC) measured at both spacecraft. We attempt to find the differences in the time center (equally divides the MC's duration into two parts), size center (equally divides the MC's size into two parts), and axis centers of the MC at the two spacecraft. We also examine the differences in the orientation of the CME flux rope axis estimated by utilizing the minimum variance analysis (MVA) technique on the observations of the two spacecraft. The multipoint in situ observations of the CME, our approach to determining the flux rope's axis, MVA analysis, and mesoscale differences in the magnetic field parameters are described in Sections 2.1 to 2.4, respectively. Section 3 summarizes our results and discusses the factors that can lead to some uncertainties in our findings.

2. Observations and Analysis Methodology

We focus on investigating the mesoscale differences in CME magnetic field and plasma parameters measured by multipoint in situ spacecraft separated by a small angular extent of around 3.4° . The in situ observations are from STEREO-A (STA) and Wind spacecraft during 2023 September 24–26. In the following, first, the in situ observations are analyzed to scrutinize the differences in the arrival times of CME substructures, such as shock, sheath, leading edge (LE), and trailing edge (TE), at the two spacecraft. The differences in the duration of CME substructures, such as sheath and MC, at both spacecraft are also estimated. Further, we focus on introducing a new approach to determining the axis of the flux rope/MC, termed the axis center, using in situ magnetic field measurements. The estimated axis center from the new approach, when compared with size and time centers, can provide insight into the compression of the MC. The orientation of the MC axis at both in situ spacecraft is estimated using the MVA technique (B. U. O. Sonnerup & L. J. J. Cahill 1967) to analyze the differences in the orientation

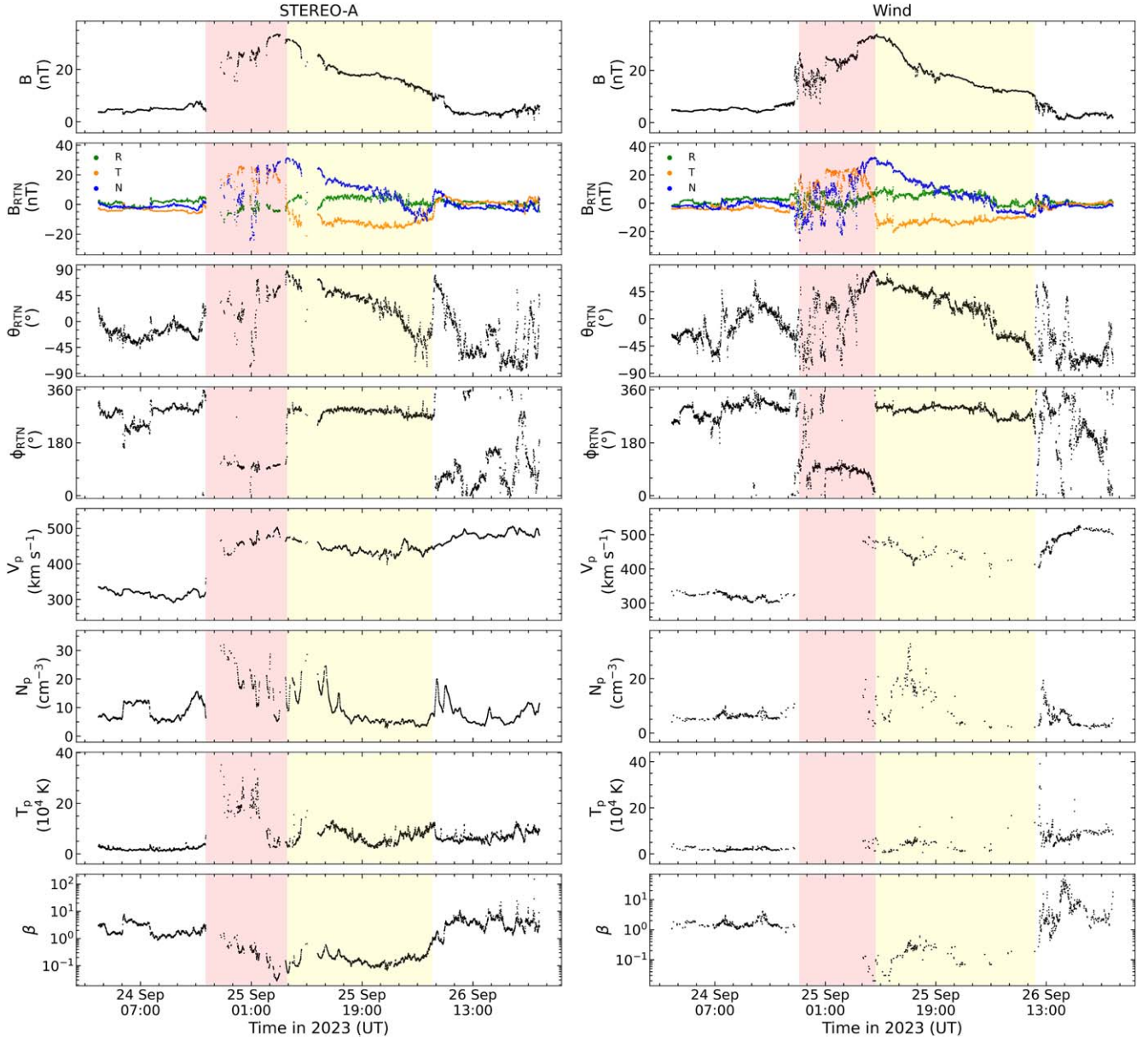


Figure 1. Panels from top to bottom show the variation of the total magnetic field, magnetic field vector in the RTN coordinate system, latitude and longitude of the total magnetic field vector, speed, density, temperature, and plasma beta, from STA and Wind in the left and right columns, respectively. Transparent areas shaded red and yellow represent the durations of the sheath and magnetic cloud during the passage of the CME at the spacecraft.

along a small angular extent of the MC. We also calculate the rms error and mean absolute error for the differences between measurements at the two spacecraft along the RTN axes and the variance axes determined by MVA. Additionally, we compute the Spearman (Pearson) correlation coefficient between measurements at the two spacecraft along these axes.

2.1. In Situ Observations of the CME Substructures at STEREO-A and Wind

The longitudinal and latitudinal separations between STA and Wind on 2023 September 25 are 3.4° and 0.1° , respectively. We scrutinize the magnetic field and plasma parameters of the selected CME for STA and Wind as depicted in the left and right columns of Figure 1, respectively. In this figure, the panels from top to bottom show the total magnetic field, radial, tangential, and normal components of the magnetic field vector (in green, orange, and blue), latitude of the total magnetic field vector (θ),

longitude of the total magnetic field vector (ϕ), speed, density, temperature, and plasma beta. We estimate θ using the total magnetic field and its normal component (B_N) as follows:

$$\theta = \sin^{-1}\left(\frac{B_N}{B}\right).$$

We estimate ϕ in the RTN coordinate system using magnetic field components B_R and B_T as follows:

If $B_R > 0$ and $B_T > 0$:

$$\phi = \tan^{-1}\left(\frac{B_T}{B_R}\right); \quad (0 < \phi < \pi/2).$$

If $B_R < 0$ and $B_T > 0$:

$$\phi = \tan^{-1}\left(\frac{B_T}{B_R}\right) + 180^\circ; \quad (\pi/2 < \phi < \pi).$$

If $B_R < 0$ and $B_T < 0$:

$$\phi = \tan^{-1}\left(\frac{B_T}{B_R}\right) + 180^\circ; (\pi < \phi < 3\pi/2).$$

If $B_R > 0$ and $B_T < 0$:

$$\phi = \tan^{-1}\left(\frac{B_T}{B_R}\right) + 360^\circ; (3\pi/2 < \phi < 2\pi).$$

The boundaries of CME substructures are identified based on their distinct signatures in the in situ observations near 1 au (T. H. Zurbuchen & I. G. Richardson 2006; I. G. Richardson & H. V. Cane 2010). However, for identifying the in situ boundaries at Wind, we primarily rely on magnetic field measurements because of the data gap in plasma measurements. The start and end boundaries of the MC at Wind are 2023 September 25 at 09:12 UT and 2023 September 26 at 11:10 UT, respectively, which are slightly different than the start (2023 September 25 at 09:00 UT) and end (2023 September 25 at 11:00 UT) boundaries of the MC in the IP CME catalog of Richardson and Cane.³ The slight difference in the selected boundaries compared to the catalog boundaries is because we strictly consider the rotation of magnetic field vectors (represented by θ and ϕ) for marking the start and end boundaries of the MC.

In Figure 1, the transparent areas shaded red and yellow depict the sheath and MC region. Also, the rotation of θ and ϕ within the MC boundary outlines the orientation of the MC as north–east–south (NES) at both spacecraft (V. Bothmer & R. Schwenn 1998). This orientation suggests that this MC is a flux rope with a low inclination whose axis is in the east direction (V. Bothmer & R. Schwenn 1998; E. Palmerio et al. 2018). The θ profile of the MC at both spacecraft shows that the rotation of θ is slow initially but suddenly decreases toward the end of the MC, and then remains nearly constant for some time. This type of variation in θ is more pronounced at Wind. Moreover, this can happen due to the compression of the MC, as reflected by the speed measurements in the MC region of the fifth panel of Figure 1. In Section 2.2, we examine the compression of the MC at both spacecraft.

Inspection of in situ measurements shows the arrival times of the shock, LE, and TE of the MC measured at STA and Wind, and the difference between the two measurements ($\Delta t = t_{\text{Wind}} - t_{\text{STA}}$), which are listed in the second, third, and fourth columns, respectively, in first panel of Table 1. We note that the arrival of CME substructures such as shock, LE, and TE at Wind is later than their arrival at STA. Such a late arrival at Wind could be due to its larger distance from the Sun than that of STA as the two spacecraft are radially separated by 0.03 au. The arrival of the shock at Wind is 3.17 hr later than its arrival at STA. We could not estimate the speed of the shock and its expected travel time from STA to Wind due to the data gap in plasma measurements at the time of shock arrival.

The arrival of the LE and TE at Wind is 2.34 hr and 4.75 hr later than their arrival at STA. Taking the measured speed of the LE and TE at STA, it is expected that they will arrive with a delay of 2.6 hr and 2.8 hr, respectively, at Wind. A longer delay in the arrival of the TE can be due to the expansion of the MC during its propagation from STA to Wind and/or a larger radial size of the cloud at Wind. However, from in situ speed measurements, we infer that this MC has negligible expansion speed, i.e., the MC is compressed, and therefore expansion

Table 1
In Situ Measurements at the Two Spacecrafts and Their Differences

Arrival Time of the CME Substructures			
Substructure	STEREO-A (UT)	Wind (UT)	Δt (hr)
Shock	24 Sep 17:35	24 Sep 20:45	3.17
LE	25 Sep 06:50	25 Sep 09:12	2.34
TE	26 Sep 06:25	26 Sep 11:10	4.75
Duration of the CME Substructures			
STEREO-A	Wind (hr)	Δt (hr)	(hr)
Sheath	13.25	12.45	−0.8
MC	23.58	25.96	2.38
Magnitude of Total Magnetic Field during the MC			
Magnetic Field	STEREO-A (nT)	Wind (nT)	ΔB (nT)
Maximum	31.6	33.9	2.3
Minimum	9.7	10	0.3
Average	18.4	18.5	0.1
Magnitude of Speed during the MC			
Speed	STEREO-A (km s ^{−1})	Wind (km s ^{−1})	ΔV (km s ^{−1})
Maximum	476	493	17
Minimum	399	378	−21
Average	442	445	3

Note. The first and second panels show the arrival time and duration of the CME substructures at STEREO-A, Wind, and the differences in measurements at the two locations. The third and fourth panels show the maximum, minimum, and average magnitudes of the magnetic field and speed during the duration of the MC at STEREO-A and Wind, along with the differences between measurements at the two locations.

cannot explain the differences in the arrival times. It appears that even a small angular separation of 3.4° between the two spacecraft has caused Wind to observe different dimensions and regions of the MC. This shows how a single-point in situ spacecraft prevents us from understanding the global plasma properties of CMEs with inhomogeneous characteristics.

The second panel of Table 1 shows the duration of the CME substructures, such as sheath and MC, measured at both spacecraft. We notice that the duration of the sheath/MC is less/more (−0.8 hr/2.37 hr) at Wind than in in situ observations at STA. The third/fourth panels show the maximum, minimum, and average magnitude of the magnetic field/speed during the duration of the MC at the two spacecraft. From this, we infer that the average values of the magnetic field at STA (18.4 nT) and Wind (18.5 nT) are close to each other. This suggests that the MC is not expanding (i.e., a compressed cloud) during its propagation of 0.03 au ($\sim 6.4 R_\odot$) distance between the two spacecraft because an expanding cloud would have shown a decrease in the total magnetic field with increasing distance (C. Wang et al. 2005; M. Leitner et al. 2007; A. M. Gulisano et al. 2010; R. M. Winslow et al. 2015; E. E. Davies et al. 2021a). In the following section, we introduce a novel approach to determining the axis of the flux rope (i.e., MC) and compare the estimates of the arrival of the axis center with those of the size center to further understand the compression of the MC.

³ <https://izw1.caltech.edu/ACE/ASC/DATA/level3/icmetable2.htm>

Table 2
Arrival Times and MVA Results

Arrival Time of Cloud Centers			
Center	STEREO-A (UT)	Wind (UT)	Δt (hr)
Size	25 Sep 18:23	25 Sep 21:55	3.54
Time	25 Sep 18:37	25 Sep 22:11	3.56
Axis	26 Sep 01:38	26 Sep 03:56	2.31

MVA Results		
Parameters	STEREO-A	Wind
Eigenvalues ($\lambda_1, \lambda_2, \lambda_3$)	(110.22, 8.45, 3.07)	(137.93, 7.27, 3.57)
λ_2/λ_3	2.75	2.04
Intermediate eigenvector (e_2)	(-0.60, 0.80, 0.01)	(-0.95, 0.17, 0.25)
Orientation (θ, ϕ) of the MC axis	(-0.7, 307°)	(-14.5, 350°)

Note. The top panel lists the arrival times of the size, time, and axis centers on STEREO-A and Wind, along with the differences between them. The bottom panel lists the result of minimum variance analysis on STEREO-A and Wind during the duration of the MC.

2.2. Proposing an Approach to Identify the Axis of the Magnetic Cloud at STEREO-A and Wind

The arrival and the orientation of the MC axis are essential parameters from the perspective of space weather. The axis center's speed and expansion govern the propagation speed of the CME LE. The axis and size centers are supposed to mark the center of the radial dimension of the flux rope at the in situ spacecraft. However, differences in the arrival times of the size and axis centers can arise if the MC undergoes compression. Recently, A. Agarwal & W. Mishra (2024) demonstrated that larger differences in the size center from the time center (marking the center of the total duration) of the MC suggest a higher expansion speed of the MC. This implies that an MC with no expansion (i.e., compression) will have no differences in the arrival times of size and time centers. One can gain insights into the compression of the MC by examining the differences in the arrival times of the axis, size, and time centers.

The radial size of the MC is estimated at the arrival of the LE by integrating the in situ speed over time during the duration of the MC. The estimated radial sizes of the MC at STA and Wind are $54.6 R_\odot$ and $59.6 R_\odot$, respectively. The arrival times of the size and time centers at STA/Wind are 2023 September 25 at 18:23/2023 September 25 at 21:55 and 2023 September 25 at 18:37/2023 September 25 at 22:11, respectively, as listed in the top panel of Table 2. The differences in the arrival of the time center from the size center at STA and Wind are 0.24 hr and 0.26 hr, respectively. This indicates that the MC is compressed as there is a negligible difference in the arrival time of size and time centers for an MC of one-day duration (A. Agarwal & W. Mishra 2024). In the following, we will introduce our approach to determine the arrival of the MC's axis and examine how different it is from the arrival of the size center.

The selected MC is a flux rope with low inclination and NES orientation, which means that the normal component of the magnetic field rotates from north (N) to south (S) via east (E). In this case, the axis of the MC will be when the normal component of the magnetic field is around zero, and the flux rope is about to change its polarity from N to S. Therefore, the

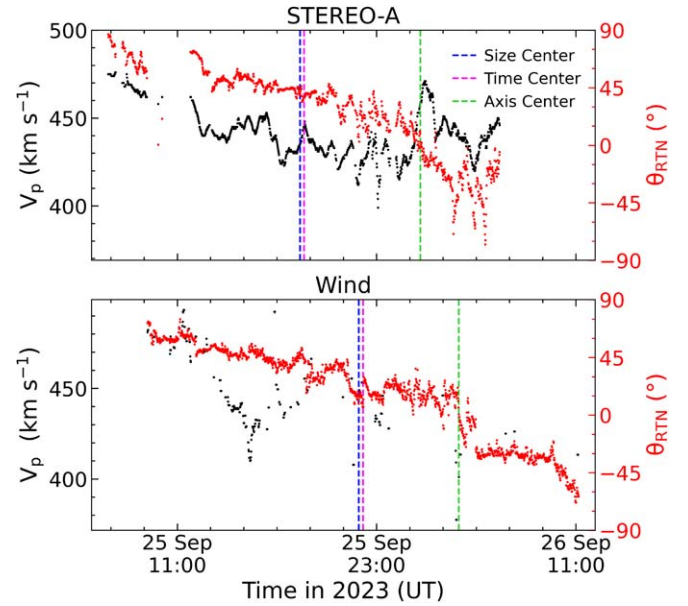


Figure 2. The in situ measured speed profiles on STA (top) and Wind (bottom) on the y-axis with black (left), while the y-axis with red (right) shows the variation in the latitude (θ) of the total magnetic field. The blue, magenta, and green vertical dashed lines denote the MC's size center, time center, and axis center.

arrival of the MC's axis (axis center) at in situ spacecraft will be at a time when the value of θ reaches nearly zero while changing its sign from “+” to “-” from the MC's LE to TE. Due to fluctuations in the measurements of 1 minute of data, it is possible to have multiple instances of θ reaching nearly zero. Therefore, in our case, we identify the axis center across which θ shows a consistent polarity for at least 15 minutes on either side. To decide on consistency in the polarity, we require that the identified polarity be satisfied for at least 80% of intervals of the selected 15 minutes on either side of the MC axis.

The selected MC is a flux rope with a low inclination; however, the method of determining the MC axis center would be equally valid on a highly inclined flux rope to understand its compression. For a highly inclined flux rope, the arrival of the MC axis can be marked utilizing the longitude (ϕ) of the magnetic field vector. For example, if the flux rope orientation is ENW, then ϕ can rotate from 270° to 90° and the MC's axis can be marked when the value of ϕ is around 180° in the RTN coordinate system.

The arrival times of the axis center at STA and Wind are 2023 September 26 at 01:38 and 2023 September 26 at 03:56, respectively, and are listed in the first panel of Table 2. The axis center arrives 2.31 hr later at Wind than at STA. The estimated arrivals of all three centers of the MC at both spacecraft are shown in Figure 2. This figure depicts the in situ speed profile in black and θ (latitude of the total magnetic field) profile in red on the left and right y-axes, respectively, for STA and Wind in the top and bottom panels. The size, time, and axis centers are denoted by blue, magenta, and green vertical dashed lines in both panels. From this figure and the top panel of Table 2, we note that the arrival of the axis center is lagging behind the size center by 7.25 hr and by 6.02 hr at STA and Wind, respectively. In the following, we illustrate the differences in the arrivals of the axis and size centers with the help of a cartoon image to give a picture of the MC compression.

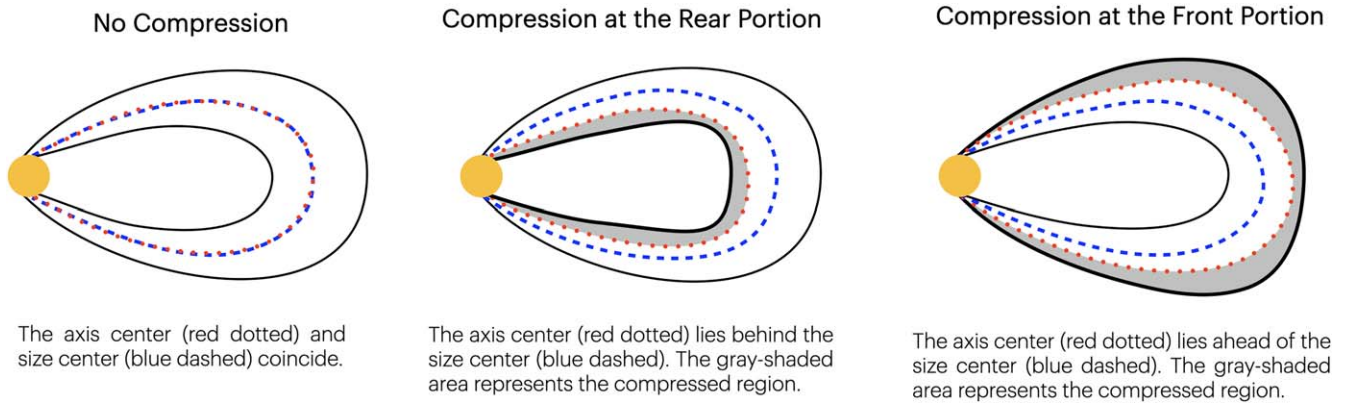


Figure 3. Cases of the MC with no compression (left), compression at the rear portion (middle), and compression at the front portion (right). The red dotted and blue dashed curved lines represent the axis center and size center of the MC. The gray shaded area represents the compressed region of the MC.

Figure 3 depicts the three scenarios of MC (flux rope) compression during its journey into the IP medium: (i) no compression, (ii) compression at the rear portion, and (iii) compression at the front portion. In each scenario, the red dotted and blue dashed curved lines denote the axis center and size center of the MC, respectively. The gray shaded region represents the compression of the MC. In the first scenario, the axis and size centers are the same when the MC is not compressed, and therefore they will arrive together at the in situ spacecraft. In the cases of compression, the arrival of size and axis centers will differ. As shown in the second scenario, where the rear portion of the MC is compressed, the size center will be ahead of the axis center. The third scenario is the compression of the MC from the front; the size center will be behind the axis center. From Figure 2, it is clear that the selected MC is compressed from the rear at both spacecraft. Compression from the rear is also clear from the speed profile of the MC region in the fifth panel of Figure 1. The greater the compression in the MC, the larger the time difference between the axis and size centers. Based on the time differences between size and axis centers, we note that compression at the rear is more pronounced at STA than at Wind even when these two spacecraft have only a small longitudinal separation of 3.4° . In the following, we will examine the orientation of the MC's axis at both spacecraft using the MVA technique (B. U. O. Sonnerup & L. J. J. Cahill 1967; V. Bothmer & R. Schwenn 1998).

2.3. Orientation of the MC Axis at STEREO-A and Wind

We determine the orientation of the axis of the MC at both spacecraft utilizing the MVA technique (B. U. O. Sonnerup & L. J. J. Cahill 1967; V. Bothmer & R. Schwenn 1998; B. U. Ö Sonnerup & M. Scheible 1998; E. Echer et al. 2006). The MVA method is a mathematical approach that involves determining the eigenvalues and eigenvectors of the magnetic variance matrix. The concepts and equations associated with the MVA technique are detailed in the Appendix for completeness. The three eigenvalues of the magnetic variance matrix $M_{\alpha\beta}$ are λ_1 , λ_2 , and λ_3 (arranged in descending order) and represent the actual maximum, intermediate, and minimum variances of the magnetic field vector in the direction of eigenvectors e_1 , e_2 , and e_3 , respectively, corresponding to each eigenvalue. The three eigenvectors are mutually orthogonal to each other. The estimated directions of variances are assumed to be well determined if $\lambda_2/\lambda_3 \geq 2$ (G. L. Siscoe &

R. W. Sney 1972; R. P. Lepping & K. W. Behannon 1980). Therefore, the smallest eigenvalue (λ_3) is equal to the minimum variance of the magnetic field vector in the direction of the normal vector ($\hat{n} [n_x, n_y, n_z]$), which is the direction of the eigenvector e_3 . The direction of the MC axis is the direction of the intermediate eigenvector e_2 .

We can compare the direction of the intermediate eigenvector or the MC's axis at multiple spacecraft and analyze the differences in the estimated direction. The estimates of eigenvalues and the intermediate eigenvector corresponding to the MC axis from the measurements of the MC at STA and Wind are given in the second panel of Table 2. From the table, we note that the ratio of intermediate to minimum eigenvalue is 2.75 and 2.04 at STA and Wind, respectively. This shows that variances are well determined, and the estimated orientation of the MC's axis at both spacecraft is reliable.

We estimate the inclination (θ) and azimuthal angle (ϕ) of the MC axis from/within the ecliptic plane at both spacecraft. For this, we use the x -, y -, and z -components of the intermediate eigenvector (e_2), which can be expressed as $e_x = e_2 \cos(\theta) \cos(\phi)$, $e_y = e_2 \cos(\theta) \sin(\phi)$, and $e_z = e_2 \sin(\theta)$, respectively. The value of ϕ ranges from 0 to 2π . We classify the value of ϕ into four ranges based on the sign of e_x and e_y simultaneously such that (i) if e_x and e_y are positive, then the value of ϕ varies from 0 to $\pi/2$; (ii) if e_x is negative and e_y is positive, then the value of ϕ varies from $\pi/2$ to π ; (iii) if e_x and e_y are negative, then the value of ϕ varies from π to $3\pi/2$; and (iv) if e_x is positive and e_y is negative, then the value of ϕ varies from $3\pi/2$ to 2π . The value of ϕ , as described above, can be mathematically calculated, and it is valid for both the geocentric solar ecliptic (GSE) and RTN coordinate systems. The mathematical expressions used for the calculation of ϕ and θ are as below:

If $e_x > 0$ and $e_y > 0$:

$$\phi = \tan^{-1}\left(\frac{e_y}{e_x}\right); \quad (0 < \phi < \pi/2).$$

If $e_x < 0$ and $e_y > 0$:

$$\phi = \tan^{-1}\left(\frac{e_y}{e_x}\right) + 180^\circ; \quad (\pi/2 < \phi < \pi).$$

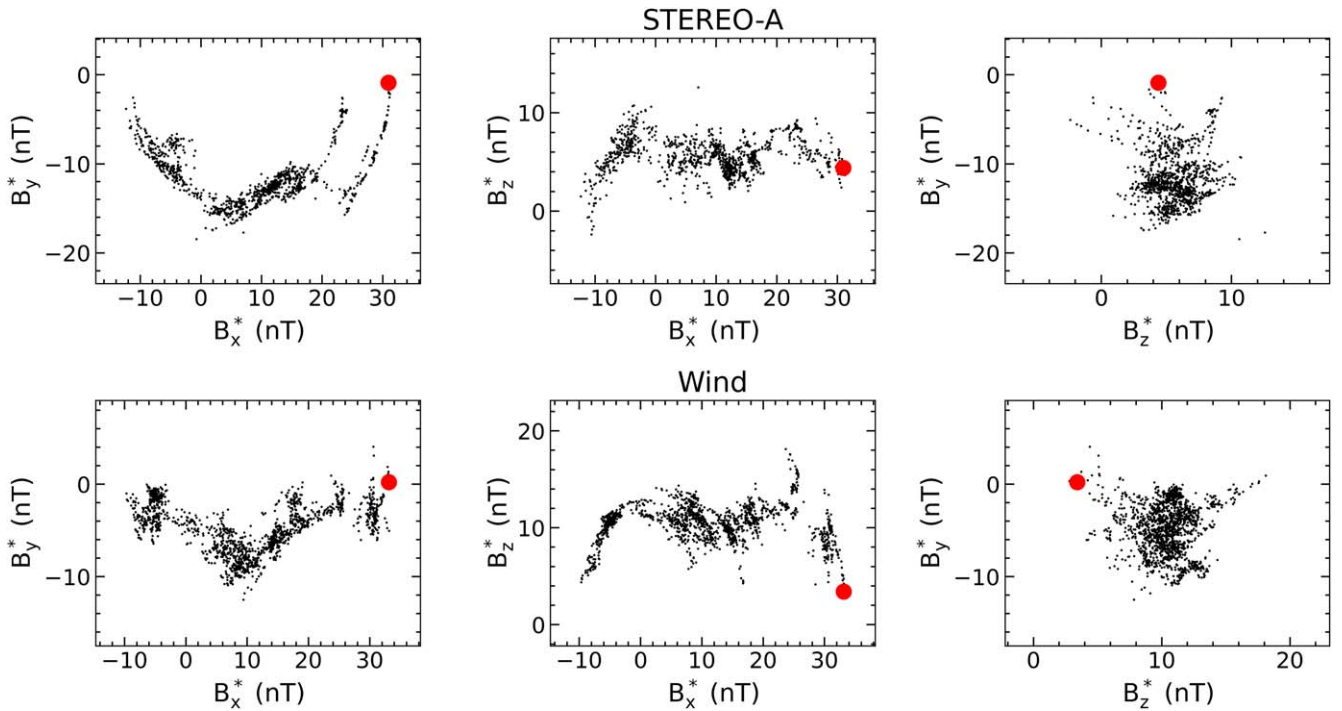


Figure 4. Hodogram representation of magnetic field vectors in the directions of maximum, intermediate, and minimum eigenvectors of STA and Wind in the top and bottom panels, respectively. The red dot represents the starting time of the MC.

If $e_x < 0$ and $e_y < 0$:

$$\phi = \tan^{-1}\left(\frac{e_y}{e_x}\right) + 180^\circ; \quad (\pi < \phi < 3\pi/2).$$

If $e_x > 0$ and $e_y < 0$:

$$\phi = \tan^{-1}\left(\frac{e_y}{e_x}\right) + 360^\circ; \quad (3\pi/2 < \phi < 2\pi)$$

$$\theta = \tan^{-1}\left(\frac{e_z}{\sqrt{e_x^2 + e_y^2}}\right).$$

The orientations (θ, ϕ) of the axis from MVA at STA and Wind are $(0.7, 127^\circ)$ and $(14.5, 170^\circ)$, respectively. The estimated value of θ at both spacecraft shows that the selected cloud of 2023 September 24–26 is a flux rope with a low inclination (V. Bothmer & R. Schwenn 1998; K. E. J. Huttunen et al. 2005; E. Palmerio et al. 2018; T. Nieves-Chinchilla et al. 2019). The estimated ϕ from MVA corresponds to the axis in the west direction at both spacecraft in the RTN system; however, the selected MC has an axis in the east direction with NES orientation as described in Section 2.1. Such ambiguity in the estimates from MVA can occur because eigenvalues of the magnetic variance matrix are always positive, as they are the actual variances in the magnetic field components (B. U. Ö. Sonnerup & M. Scheible 1998; R. A. Rosa Oliveira et al. 2021) and the eigenvectors e and $-e$ both are valid. To make the orientation of the MC's axis estimated from MVA consistent with in situ measurements, we added 180° in the estimates of ϕ and also reversed the sign of θ , which amounts to the same as reversing the sign of e_2 from MVA representing the MC axis. Thus, the modified and actual orientations (θ, ϕ) of the MC's axis in 3D space at STA and Wind are $(-0.7, 307^\circ)$ and $(-14.5, 350^\circ)$, respectively.

From the estimated θ , we note that the MC lies completely in the ecliptic plane for STA with $\theta = -0.7$ compared to $\theta = -14.5$ at the Wind spacecraft. The estimated value of ϕ shows that the orientation of the axis is not exactly aligned with the east direction ($\phi = 270^\circ$) at both spacecraft. For STA, the MC axis ($\phi = 307^\circ$) is 37° away from the east axis, while for Wind, the MC axis ($\phi = 350^\circ$) is 80° away from the east axis and more toward the Sun–Earth axis. From MVA, we note the differences in the MC's axis orientation even for 3.4 longitudinally separated spacecraft. This suggests that there would also be differences in the orientation of vectors corresponding to maximum and minimum variances at both spacecraft. One can examine the magnetic field vector in the directions of maximum, intermediate, and minimum variances at both spacecraft using the hodogram representation, which is shown in Figure 4.

The top and bottom panels of the figure illustrate the hodogram representation for STA and Wind, respectively. B_x^* , B_y^* , and B_z^* denote the magnetic field vector in the directions of maximum, intermediate, and minimum eigenvectors, respectively. The red dot represents the start time of the MC. Due to the ambiguity in the sign of eigenvectors, although they satisfy a right-hand coordinate system, the hodogram representation can show different types of orientation of the MC's axis. For the flux rope axis with a low inclination, as for the selected MC in this study, the ambiguity in eigenvectors can show four types of orientation: NES, SEN, SWN, and NWS in the hodogram. For our selected MC, we have taken the sign of eigenvectors such that they become the correct choice for NES orientation as identified in Section 2.1. Such ambiguities in the hodogram and the possible solutions for them, based on the inputs of latitude and longitude of the magnetic field vector during the duration of the MC, are discussed by R. A. Rosa Oliveira et al. (2021).

The hodogram consistent with NES orientation at both spacecraft is shown in Figure 4. The hodogram between B_y^* and B_x^* shows a clear rotation in B_x^* from positive to negative as the

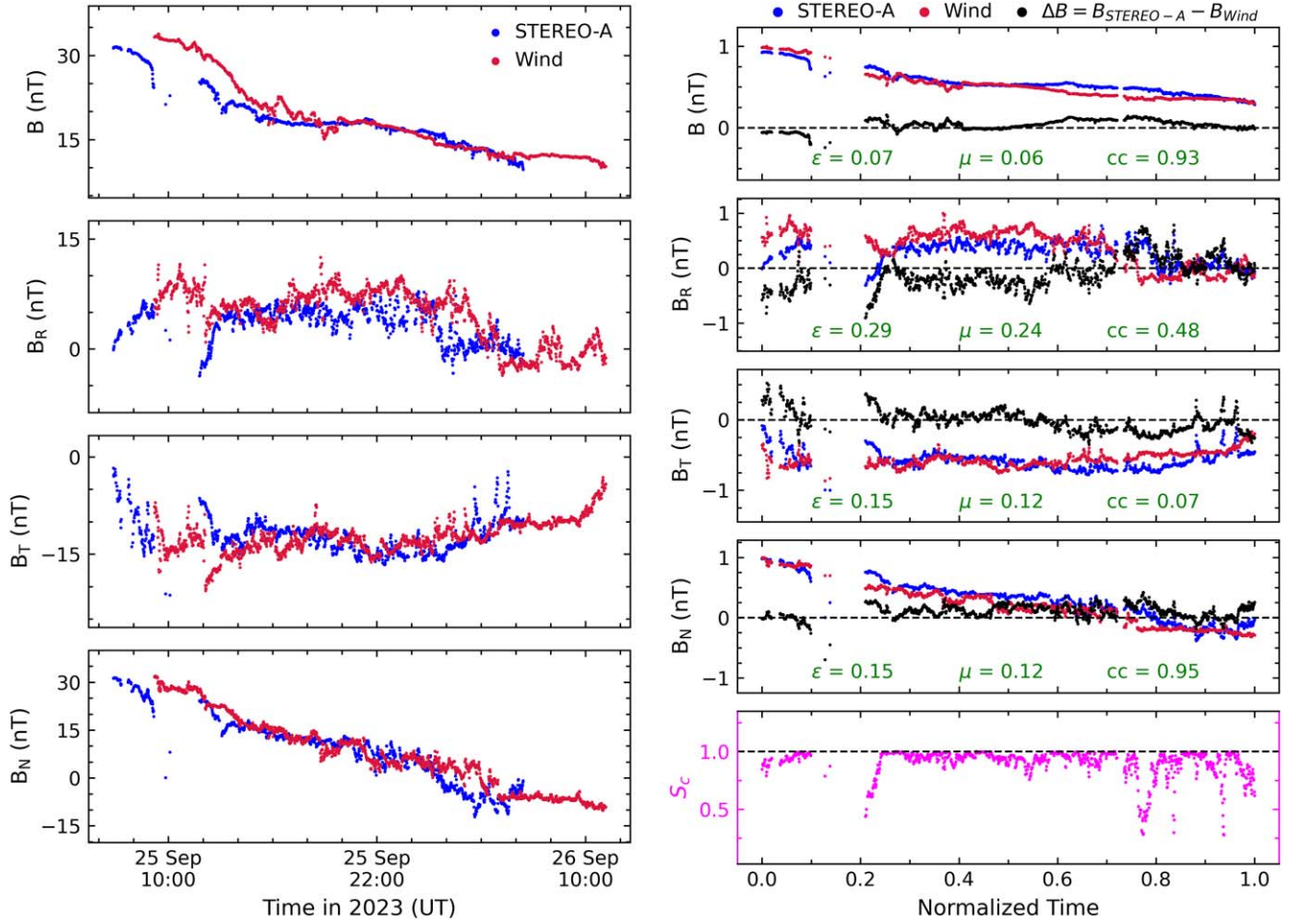


Figure 5. Left panels: the temporal evolution of the total magnetic field and its components in the RTN coordinate system at STA (blue) and Wind (red). Right panels: the first four panels on the right show the variations in the normalized total magnetic field and its normalized components corresponding to STA (blue) and Wind (red), along with their differences ($\Delta B = B_{\text{STA}} - B_{\text{Wind}}$) (black) as a function of the normalized time of the MC duration. Each panel includes the Spearman correlation coefficient (cc) between measurements at STA and Wind as well as rms error (ϵ) and mean absolute error (μ) for ΔB , reported in green text. The last panel of the figure shows the cosine similarity ($S_c = \cos(\theta)$) between magnetic field vectors at STA and Wind over the normalized time of the MC duration.

value of B_y^* changes while maintaining its negative sign at both spacecraft; however, the rotation is more pronounced at STA. The second hodogram between B_z^* and B_x^* shows the change in the value of B_x^* from positive to negative with the nearly constant value of B_z^* for STA, while the value of B_z^* shows some variation at Wind. The third hodogram between B_y^* and B_z^* shows the change in the value of B_y^* while maintaining its negative sign with the nearly constant value of B_z^* for STA, while the value of B_z^* shows some variation at Wind. This suggests that the MC axis is slightly inclined away from the ecliptic plane at Wind but is exactly in the ecliptic plane at STA. Two spacecraft detecting a slightly different orientation of the MC despite their much smaller separation of around $3.^\circ 4$ provides insights into the local inhomogeneity in the MC either inherently present or arising during its propagation in the nonisotropic ambient medium. In the following, we will examine the magnetic field parameters on both spacecraft.

2.4. Comparison of Magnetic Field Profiles Observed at STEREO-A and Wind

We note a similar trend in the time evolution of the total magnetic field and closely matching values of its maximum,

minimum, and average at both STA and Wind spacecraft over the MC duration (Section 2.1). However, its RTN components at both spacecraft show noticeable differences, especially toward the trailing edge of the MC, as shown in the left panel of Figure 5. This suggests that differences in RTN components of the field between the two spacecraft may not be primarily due to its temporal evolution between them given a radial separation of only 0.03 au ($\sim 6.4 R_\odot$). Based on our earlier analysis of differing arrival times of centers and orientation of the MC at the two spacecraft, we think the measured differences could be because of noncoherency in the MC structure over a small spatial scale separated by an angular extent of $3.^\circ 4$.

It is clear from the left panels of Figure 5 that the two spacecraft are not sampling the LE and TE at common times and measure different durations of the MC. Therefore, we normalize the MC duration for both spacecraft to enable a one-to-one comparison between them of the temporal evolution of the magnetic field. The normalized time for the duration of the MC at both spacecraft is calculated as follows:

$$t_{\text{norm}} = \frac{t - t_{\text{start}}}{t_{\text{end}} - t_{\text{start}}}.$$

For quantifying the differences between the magnetic field parameters at the two spacecraft at a common normalized time,

we interpolate the measurements of Wind (having a larger number of data points) at the normalized time of STA. Additionally, to have an easy comparison between each magnetic field parameter, we normalize it by an absolute maximum of its measurements at both spacecraft. The right panel of Figure 5 shows the comparison of magnetic field parameters at both spacecraft with normalized time. The normalized magnetic field and its components at STA and Wind are shown in blue and red, respectively, in the first four panels of the figure. The difference ($\Delta B = B_{\text{STA}} - B_{\text{Wind}}$) between measurements from the two spacecraft is shown in black. The horizontal black dashed line represents the zero reference to visualize the variation of ΔB . We also compute the rms error (ϵ) and mean absolute error (μ) for ΔB as follows:

$$\epsilon = \sqrt{\frac{\sum_{i=1}^N (\Delta B_i)^2}{N}}$$

$$\mu = \frac{\sum_{i=1}^N |\Delta B_i|}{N}.$$

We note that the values of ϵ and μ are smaller for the total magnetic field than their values for the RTN components of the field, as reported in green text in each panel. The values of ϵ and μ are highest for the radial component of the magnetic field, while they are equal for the tangential and normal components. The variation of ΔB for the total magnetic field relative to the zero reference line shows moderately non-identical values at both spacecraft for approximately one-third of the magnetic cloud (MC) during the 60%–90% trailing portion of its duration. The variation of ΔB_R shows that B_R at the two spacecraft is significantly different for the whole duration of the MC, except for the one-tenth portion from 60%–70% of the normalized MC duration. B_T is noted to be moderately nonidentical at both spacecraft only for the first 10% and the last 30% portion of the MC duration. ΔB_N and the zero line are closely related during the whole duration of the MC. We also calculated the values of ϵ and μ after excluding a few visually noticeable fluctuations as outliers, especially around the data gap, and found that their values remained largely unaffected, indicating that these parameters reliably quantify the overall differences between the two profiles.

We check the Spearman (Pearson) correlation coefficient (cc) between the normalized magnetic field profiles at the two spacecraft. Such an approach is also taken by S. W. Good et al. (2018). We infer that the values of Spearman (Pearson) cc for the total magnetic field and normal component of the magnetic field are 0.93 (0.95) and 0.95 (0.94), respectively, suggesting that measurements of these parameters at both spacecraft are highly correlated with a monotonic (linear) relationship. The values of Spearman (Pearson) cc for the radial and tangential components of the magnetic field are 0.48 (0.56) and 0.07 (0.15), respectively. The low value of cc for the tangential component could also result from the smaller variations in the magnitude of B_T at each spacecraft, and in such cases the cc value may not be suitable for identifying the dissimilarity. The Spearman cc is reported in green text in the panels on the right of Figure 5. Overall, the analysis suggests that the magnetic field parameters of the MC are different between STA and Wind measurements.

Further, we examine the directional similarity of the magnetic field vector at both spacecraft using the cosine similarity. The cosine similarity (S_c) is defined as a cosine of

the angle between the magnetic field vector measured at STA (B_{STA}) and at Wind (B_{Wind}) as follows:

$$S_c = \cos(\theta) = \frac{B_{\text{STA}} \cdot B_{\text{Wind}}}{|B_{\text{STA}}| |B_{\text{Wind}}|}.$$

The value of S_c can vary from -1 to 1 . Values of $S_c = 1$, 0 , and -1 imply that both vectors are exactly aligned in the same direction, orthogonal, and exactly oppositely oriented, respectively. The value of S_c is shown in the bottom panel of the right-hand side Figure 5 in magenta as a function of normalized time of the MC duration. The horizontal black dashed line shows $S_c = 1$ as a reference for visualizing the variation above and below it. We note that the value of S_c is close to 1 for most of the MC duration except for the last 20% at the trailing portion. It shows that the orientation of the magnetic field vector at the two spacecraft differs at the trailing portion of the MC, which is consistent with inference from ΔB_R and ΔB_T . This suggests the flux rope structure is noncoherent, primarily at its trailing portion. This is also in agreement with the inferred MC compression from the rear, as discussed in Section 2.2.

We also attempt to investigate the differences in the magnetic field components in the directions of minimum (B_z^*), intermediate (B_y^*), and maximum (B_x^*) variance (from MVA) at STA and Wind, as shown in the left panels of Figure 6. The first three panels on the right of the figure show the normalized field parameters in the direction of different variance axes for STA (blue) and Wind (red). The difference ($\Delta B^* = B_{\text{STA}}^* - B_{\text{Wind}}^*$) in these parameters are shown in black. The normalized components of the field and time are estimated using a similar approach to that described above for the measured magnetic field components in the RTN coordinate system. The estimated values of ϵ and μ for the difference in the components are reported in green text in each panel. From this, we note that these values are smaller for ΔB_x^* than for ΔB_y^* and ΔB_z^* . However, the values of ϵ and μ are largest for ΔB_y^* . This suggests that the direction of the MC axis at the two spacecraft is different, even when the angular separation between them is 3.4° , which is expected from Section 2.3. This also shows that the direction of minimum variance within the MC is significantly different for the two spacecraft.

The horizontal black dashed line in the figure represents the zero reference line for ΔB^* . From this, we infer that B_z^* and B_y^* are different at the two spacecraft over the whole duration of the MC. However, B_x^* at the two spacecraft is similar over the MC duration. The values of Spearman (Pearson) cc for B_z^* , B_y^* , and B_x^* are 0.19 (0.13), 0.34 (0.34), and 0.95 (0.95). The value of cc is highest for B_x^* in agreement with the smallest value of ϵ and μ . The low value of cc for B_z^* and B_y^* could be because of the larger values of ϵ and μ as well as relatively constant magnitudes of B_z^* and B_y^* at both spacecraft. We also estimate S_c (for directional similarity) between magnetic field vectors at both spacecraft comprising B_z^* , B_y^* , and B_x^* . The horizontal black dashed line represents the value of $S_c = 1$. We infer that the direction of the total magnetic field vector, based on its components in the direction of variances, at both spacecraft is nonidentical during the last 40% of the MC. This can happen due to the compression of the MC from the rear, as discussed in Section 2.2.

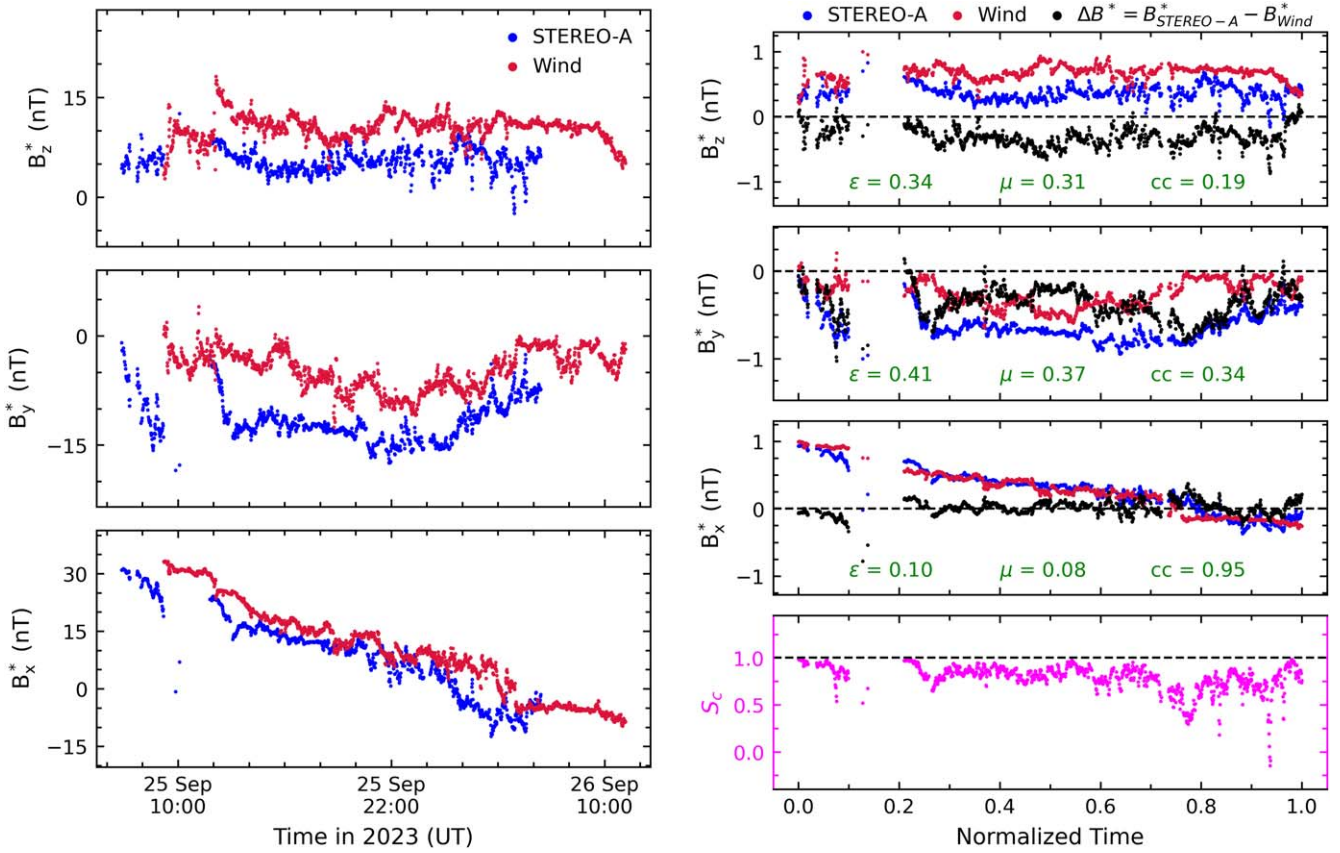


Figure 6. Left panels: the temporal evolution of the magnetic field vector in the directions of minimum (top), intermediate (middle), and maximum (bottom) variance at STA (blue) and Wind (red). Right panels: the first three panels on the right show the variations in the normalized components corresponding to STA (blue) and Wind (red), along with their differences ($\Delta B^* = B_{STA}^* - B_{Wind}^*$) (black) as a function of the normalized time of the MC duration. Each panel includes the Spearman correlation coefficient (cc) between measurements at STA and Wind as well as rms error (ϵ) and mean absolute error (μ) for ΔB^* , reported in green text. The last panel of the figure shows the cosine similarity ($S_c = \cos(\theta)$) between magnetic field vectors, based on its components, in the directions of minimum, intermediate, and maximum variance at STA and Wind over the normalized time of the MC duration.

3. Results and Discussion

The present study focuses on analyzing the observations of a selected CME at two closely spaced in situ spacecraft near 1 au and examining the differences in the characteristics of the CME measured at the two locations. The selected CME was observed at STA and Wind spacecraft during 2023 September 24–26, with minimal radial and longitudinal separations between the spacecraft of 0.03 au and 3.4° , respectively. Such unique locations of both spacecraft place them in a rare conjunction and enable mesoscale observations of the CME. We estimate the arrival times of CME substructures (shock, LE, and TE), MC axis, and MC orientation at STA and Wind and compare the estimates for both locations. We also compare the trends of variations in the magnetic field parameters within the MC duration for both locations. Such a comparison of multipoint measurements on a small scale provides insights into inhomogeneity within the CME, which could be a consequence of its kinematic deformation or its noncoherent structure during its propagation in the nonuniform solar wind (M. J. Owens et al. 2017; N. Al-Haddad & N. Lugaz 2025).

We identify the MC’s axis (i.e., axis center) by employing a relatively unexplored method that utilizes the variations in the latitude/longitude of the total magnetic field over the MC duration. The arrival time estimates of the axis center and size center of the MC at any spacecraft help us to understand its compression at the front/rear portion of the MC. Moreover,

comparing these centers on the two longitudinally separated spacecraft can shed light on the compression of the MC along its angular extent. The asynchrony between the axis and size centers of the MC at the two spacecraft suggests the compression of the MC (Figure 2). The axis center is lagging behind the size center of the MC by 7.25 and 6.02 hr at STA and Wind, respectively. A larger time difference between the arrival of the axis center and the size center would suggest a more substantial compression of the CME, resulting in its deformation. This suggests that the MC at both spacecraft is compressed from the rear, and more strongly at STA than at Wind. The compression of CMEs/MCs has also been previously noted because of their interaction with following faster solar wind, CMEs, and shocks (W. Mishra & N. Srivastava 2014; M. Temmer et al. 2014; W. Mishra et al. 2015; S. G. Heinemann et al. 2019). The compression of the selected MC is also evident as the time center and size center are synchronous at both spacecraft (Figure 2). The compression of the MC inferred from the asynchrony between the axis and size centers is illustrated in Figure 3. The study of R. M. Winslow et al. (2021) has reported the compression in an MC observed at PSP and STA, which were separated radially and longitudinally by 0.19 au and 8° , respectively. Their study did not find the compression of the MC along its angular extent. However, we find evidence of nonisotropic compression for the selected MC and suggest such a possibility even at the mesoscale.

The multipoint in situ measurements of the selected CME/MC show that the arrival of its substructures (shock, LE, and TE) at Wind is later than their arrival at STA due to the small radial separation of 0.03 au ($\sim 6.4 R_{\odot}$) between the two spacecraft. The arrival of the TE at Wind is significantly later than the arrival of other substructures. This implies a larger radial size of the MC at Wind ($59.6 R_{\odot}$) than at STA ($54.6 R_{\odot}$), possibly due to a weaker compression or lesser deformation at Wind. Our finding suggests that even a small angular separation of 3.4° between two spacecraft can cause them to detect radial sizes differing by 10%. Our finding is important as the two spacecraft are almost in the same plane, and they are likely to have the same crossing distance from the MC axis. The differences in the detected radial sizes of the CMEs/MCs at multiple spacecraft have been noted in earlier studies, particularly for spacecraft having larger radial/longitudinal separations between them (N. U. Crooker & D. S. Intriligator 1996; M. Leitner et al. 2007; N. Lugaz et al. 2020).

We further employ the MVA on magnetic field parameters and determine the orientation of MC's axis at both spacecraft. The orientations (θ , ϕ) of the axis at STA and Wind, consistent with NES orientation, are $(-0.7^{\circ}, 307^{\circ})$ and $(-14.5^{\circ}, 350^{\circ})$, respectively. The small angular separation of even 3.4° between the two in situ spacecraft could show such a difference in the MC's axis orientation. The orientation of the MC is slightly out of the ecliptic at Wind, and its effect reduces the sampled radial size (N. U. Crooker & D. S. Intriligator 1996; V. Bothmer & R. Schwenn 1998), which contrasts with our finding. Therefore, we think that the effect of nonisotropic compression is larger than that of the orientation of the MC axis in governing the measured radial sizes at the two spacecraft. From the hodogram representation (Figure 4) consistent with NES orientation, we note a clear rotation in B_x^* for the hodogram between B_y^* and B_x^* at both spacecraft; however, the rotation is more evident for STA. The hodogram between B_z^* and B_x^* depicts a minimal rotation in B_x^* only for Wind and not for STA, which is expected. Similar to our study, Y. Liu et al. (2008) also note the discernible differences in the orientation of the 2007 May MC observed by the twin STEREO and Wind, which had a small angular separation between them.

The comparison between magnetic field parameters at both spacecraft shows the noticeable differences in radial and tangential components of the magnetic field, especially during the trailing portion of the MC. Also, analysis of the cosine similarity suggests that the direction of the magnetic field vector at both spacecraft is different in the trailing part of the MC. This could be possible due to the compression of the MC from the rear. The total magnetic field and its normal component at both spacecraft exhibit a strong correlation. Additionally, the magnetic field vector in the direction of the intermediate variance axis at both spacecraft shows significant differences in comparison to the magnetic field vector in the direction of minimum and maximum variance, consistent with the axis orientation from the MVA analysis. The analysis of cosine similarity between the magnetic field vectors in the direction of variance axes at the two spacecraft reveals the vectors are in different directions, significantly in the trailing part of the MC. From this analysis, we identify noncoherency in the magnetic field structure in the trailing part of the MC, which could be possible because of compression at the rear or can be inherent. However, we note that our analysis can have biases due to the inherent limitations of 1D in situ

measurements, which have difficulty capturing the full complexity of a 3D structure of an MC. Also, the findings from the MVA method have uncertainties due to changes in the identified boundaries and duration of the MC (R. A. Rosa Oliveira et al. 2021).

Our study established that even for a small angular separation of 3.4° between the multipoint in situ spacecraft, the plasma and magnetic field parameters of an MC are anisotropic or inhomogeneous at the mesoscale along its angular extent. This finding could be due to the influence of the nonuniform ambient medium on the MC or the inherent noncoherent flux rope structure in the MC itself. We emphasize that plasma measurements of the MC taken by a single-point in situ spacecraft could not represent the global properties of CMEs. Similar to our study, earlier studies also reported differences in the magnetic field properties of the MC along its small angular extent (E. K. J. Kilpua et al. 2011; N. Lugaz et al. 2018). Also, the study of F. Regnault et al. (2024) found notable changes in both the magnetic field and the speed of an MC observed by SolO and Wind, which were separated radially by 0.13 au and longitudinally by 2.2° . Our study additionally notes a nonisotropic compression along the angular extent of the MC, which is not present in the case study of F. Regnault et al. (2024). Our findings offer an alternative perspective to that of R. M. Winslow et al. (2021), which reported a uniform distortion of an MC over a comparatively larger angular extent of around 8° . Our study contributes a case study to the existing literature, supporting the idea that MC observations observed by a single in situ spacecraft reflect local characteristics rather than global ones (C. Möstl et al. 2012; W. Mishra et al. 2021a; N. Lugaz et al. 2022).

The study of E. E. Davies et al. (2020) found that the MC properties measured from near-Earth spacecraft (Wind, ACE, THEMIS B, and THEMIS C having mutual separations smaller than 0.01 au and 0.2°) have no considerable changes in the magnetic field parameters of an MC along its small angular extent. Therefore, in the context of our study, it would be important to understand the scales over which the MC characteristics could be assumed to be the same. The observed differences in the orientation of the MC at various locations suggest that longitudinal separation, rather than radial separation between the spacecraft, predominantly influences the magnetic field properties. Our study highlights that a few MCs could exhibit inhomogeneity in their properties along a small angular extent.

Our study shows the mesoscale differences of the CME observed on 2023 September 24–26 at STA and Wind near 1 au distance from the Sun. This study shows the necessity of more multipoint in situ spacecraft studies along the angular extent of the CME to further understand the physical processes responsible for inhomogeneity at different scales within CME. Future studies making statistics of such CMEs observed by multiple spacecraft separated by much smaller distances and longitudes will help understand whether most CMEs have appreciable inhomogeneity at mesoscales because of the flux rope's noncoherent structure. Also, the role of interactions between CMEs and surrounding nonuniform ambient medium needs to be examined to get insights into the growth of an existing inhomogeneity in CMEs at different scales. Therefore, a comprehensive understanding of the global characteristics of MCs requires coordinated multispacecraft observations of the

same MC across its angular extent from regions near the Sun through interplanetary space.

Acknowledgments

We thank the STEREO (IMPACT and PLASTIC) and Wind (MFI and SWE) spacecraft team members for making their observations publicly available. We also thank the anonymous referee for careful review that improved the manuscript.

Facilities: STEREO, Wind.

Appendix Minimum Variance Analysis

The MVA technique is used to determine the direction in space in which the magnetic field vector over the complete duration of the MC has a minimum variance. This implies that the technique determines the normal vector (\hat{n} [n_x, n_y, n_z]) such that the in situ measured magnetic field vector ($\mathbf{B}^{(i)}$) projected along the normal direction ($\mathbf{B}^{(i)} \cdot \hat{n}$) will have minimum variance, where \mathbf{B} represents the measured components of the magnetic field vector (B_x, B_y, B_z) in the Cartesian coordinate system (e.g., GSE or RTN) at times $i = 1, 2, \dots, N$ during the passage of the MC at the spacecraft. The minimization of variance estimates the normal vector for the magnetic field vectors in the normal direction ($\mathbf{B}^{(i)} \cdot \hat{n}$) under the constraint $|\hat{n}|^2 = 1$. Thus, the variance can be written as follows:

$$\sigma^2 = \frac{1}{N} \sum_{i=1}^N |(\mathbf{B}^{(i)} - \langle \mathbf{B} \rangle) \cdot \hat{n}|^2, \quad (\text{A1})$$

where $\langle \mathbf{B} \rangle$ represents the average of $\mathbf{B}^{(i)}$ over the duration of the MC, i.e.,

$$\langle \mathbf{B} \rangle = \frac{1}{N} \sum_{i=1}^N \mathbf{B}^{(i)}.$$

The minimization of variance under the constraint of the normal vector ($|\hat{n}|^2 - 1 = 0$) has been estimated using a Lagrange multiplier λ . This reduces to estimating the solution of the three homogeneous linear Equations (A2), (A3), and (A4) as given below:

$$\frac{\partial}{\partial n_x} [\sigma^2 - \lambda(|\hat{n}|^2 - 1)] = 0 \quad (\text{A2})$$

$$\frac{\partial}{\partial n_y} [\sigma^2 - \lambda(|\hat{n}|^2 - 1)] = 0 \quad (\text{A3})$$

$$\frac{\partial}{\partial n_z} [\sigma^2 - \lambda(|\hat{n}|^2 - 1)] = 0. \quad (\text{A4})$$

We further expand Equation (A1) for completeness in the literature as follows:

$$\begin{aligned} \sigma^2 = & \frac{1}{N} \sum_{i=1}^N [(B_x^{(i)} - \langle B_x \rangle)^2 n_x^2 + (B_y^{(i)} - \langle B_y \rangle)^2 n_y^2 \\ & + (B_z^{(i)} - \langle B_z \rangle)^2 n_z^2 \\ & + 2(B_x^{(i)} - \langle B_x \rangle)(B_y^{(i)} - \langle B_y \rangle) n_x n_y \\ & + 2(B_x^{(i)} - \langle B_x \rangle)(B_z^{(i)} - \langle B_z \rangle) n_x n_z \\ & + 2(B_y^{(i)} - \langle B_y \rangle)(B_z^{(i)} - \langle B_z \rangle) n_y n_z] \end{aligned}$$

$$\begin{aligned} \sigma^2 = & (\langle B_x B_x \rangle - \langle B_x \rangle \langle B_x \rangle) n_x^2 \\ & + (\langle B_y B_y \rangle - \langle B_y \rangle \langle B_y \rangle) n_y^2 \\ & + (\langle B_z B_z \rangle - \langle B_z \rangle \langle B_z \rangle) n_z^2 \\ & + 2(\langle B_x B_y \rangle - \langle B_x \rangle \langle B_y \rangle) n_x n_y \\ & + 2(\langle B_x B_z \rangle - \langle B_x \rangle \langle B_z \rangle) n_x n_z \\ & + 2(\langle B_y B_z \rangle - \langle B_y \rangle \langle B_z \rangle) n_y n_z. \end{aligned} \quad (\text{A5})$$

Using Equation (A5), Equations (A2), (A3), and (A4) can also be written as follows:

$$\begin{aligned} (\langle B_x B_x \rangle - \langle B_x \rangle \langle B_x \rangle) n_x + (\langle B_x B_y \rangle - \langle B_x \rangle \langle B_y \rangle) n_y \\ + (\langle B_x B_z \rangle - \langle B_x \rangle \langle B_z \rangle) n_z = \lambda n_x \end{aligned} \quad (\text{A6})$$

$$\begin{aligned} (\langle B_x B_y \rangle - \langle B_x \rangle \langle B_y \rangle) n_x + (\langle B_y B_y \rangle - \langle B_y \rangle \langle B_y \rangle) n_y \\ + (\langle B_y B_z \rangle - \langle B_y \rangle \langle B_z \rangle) n_z = \lambda n_y \end{aligned} \quad (\text{A7})$$

$$\begin{aligned} (\langle B_x B_z \rangle - \langle B_x \rangle \langle B_z \rangle) n_x + (\langle B_y B_z \rangle - \langle B_y \rangle \langle B_z \rangle) n_y \\ + (\langle B_z B_z \rangle - \langle B_z \rangle \langle B_z \rangle) n_z = \lambda n_z. \end{aligned} \quad (\text{A8})$$

The above Equations (A6), (A7), and (A8) can be represented in a matrix form as shown below:

$$\sum_{\beta=1}^3 M_{\alpha\beta} n_\beta = \lambda n_\alpha, \quad (\text{A9})$$

where $M_{\alpha\beta} = \langle B_\alpha B_\beta \rangle - \langle B_\alpha \rangle \langle B_\beta \rangle$ and $\alpha, \beta = 1, 2, 3$, which represent the x -, y -, and z -components of the Cartesian coordinate system.

ORCID iDs

Anjali Agarwal  <https://orcid.org/0009-0007-4956-5108>
Wageesh Mishra  <https://orcid.org/0000-0003-2740-2280>

References

- Agarwal, A., & Mishra, W. 2024, *MNRAS*, **534**, 2458
Al-Haddad, N., & Lugaz, N. 2025, *SSRv*, **221**, 12
Bothmer, V., & Schwenn, R. 1998, *AnGeo*, **16**, 1
Burlaga, L., Sittler, E., Mariani, F., & Schwenn, R. 1981, *JGR*, **86**, 6673
Cremades, H., Iglesias, F. A., & Merenda, L. A. 2020, *A&A*, **635**, A100
Crooker, N. U., & Intriligator, D. S. 1996, *JGR*, **101**, 24343
Davies, E. E., Forsyth, R. J., Good, S. W., & Kilpua, E. K. J. 2020, *SoPh*, **295**, 157
Davies, E. E., Forsyth, R. J., Winslow, R. M., Möstl, C., & Lugaz, N. 2021a, *ApJ*, **923**, 136
Davies, E. E., Möstl, C., Owens, M. J., et al. 2021b, *A&A*, **656**, A2
Davies, J. A., Perry, C. H., Trines, R. M. G. M., et al. 2013, *ApJ*, **777**, 167
Desai, R. T., Zhang, H., Davies, E. E., et al. 2020, *SoPh*, **295**, 130
Echer, E., Gonzalez, W. D., & Alves, M. V. 2006, *SoPh*, **233**, 249
Galvin, A. B., Kistler, L. M., Popecki, M. A., et al. 2008, *SSRv*, **136**, 437
Gonzalez, W. D., Tsurutani, B. T., & Clúa de Gonzalez, A. L. 1999, *SSRv*, **88**, 529
Good, S. W., Forsyth, R. J., Eastwood, J. P., & Möstl, C. 2018, *SoPh*, **293**, 52
Good, S. W., Forsyth, R. J., Raines, J. M., et al. 2015, *ApJ*, **807**, 177
Gopalswamy, N. 2006, *SSRv*, **124**, 145
Gopalswamy, N., Mäkelä, P., Xie, H., Akiyama, S., & Yashiro, S. 2009, *JGRA*, **114**, A00A22
Gosling, J. T. 1990, *GMS*, **58**, 343
Gulisano, A. M., Démoulin, P., Dasso, S., Ruiz, M. E., & Marsch, E. 2010, *A&A*, **509**, A39
Heinemann, S. G., Temmer, M., Farrugia, C. J., et al. 2019, *SoPh*, **294**, 121
Howard, R. A., Moses, J. D., Vourlidis, A., et al. 2008, *SSRv*, **136**, 67
Huttunen, K. E. J., Schwenn, R., Bothmer, V., & Koskinen, H. E. J. 2005, *AnGeo*, **23**, 625
Kaiser, M. L., Kucera, T. A., Davila, J. M., et al. 2008, *SSRv*, **136**, 5
Kay, C., & Nieves-Chinchilla, T. 2021, *JGRA*, **126**, e28966
Khuntia, S., Mishra, W., Mishra, S. K., et al. 2023, *ApJ*, **958**, 92
Kilpua, E. K. J., Good, S. W., Dressing, N., et al. 2021, *A&A*, **656**, A8

- Kilpua, E. K. J., Good, S. W., Palmerio, E., et al. 2019, *FrASS*, **6**, 50
- Kilpua, E. K. J., Jian, L. K., Li, Y., Luhmann, J. G., & Russell, C. T. 2011, *JASTP*, **73**, 1228
- Leitner, M., Farrugia, C. J., Möstl, C., et al. 2007, *JGRA*, **112**, A06113
- Lepping, R. P., & Behannon, K. W. 1980, *JGR*, **85**, 4695
- Liu, Y., Luhmann, J. G., Huttunen, K. E. J., et al. 2008, *ApJL*, **677**, L133
- Liu, Y., Richardson, J. D., & Belcher, J. W. 2005, *P&SS*, **53**, 3
- Lugaz, N., Farrugia, C. J., Winslow, R. M., et al. 2018, *ApJL*, **864**, L7
- Lugaz, N., Salman, T. M., Zhuang, B., et al. 2022, *ApJ*, **929**, 149
- Lugaz, N., Winslow, R. M., & Farrugia, C. J. 2020, *JGRA*, **125**, e27213
- Luhmann, J. G., Curtis, D. W., Schroeder, P., et al. 2008, *SSRv*, **136**, 117
- Mishra, W., Dave, K., Srivastava, N., & Teriaca, L. 2021a, *MNRAS*, **506**, 1186
- Mishra, W., Doshi, U., & Srivastava, N. 2021b, *FrASS*, **8**, 142
- Mishra, W., & Srivastava, N. 2014, *ApJ*, **794**, 64
- Mishra, W., & Srivastava, N. 2015, *JWSC*, **5**, A20
- Mishra, W., Srivastava, N., & Singh, T. 2015, *JGRA*, **120**, 10,221
- Mishra, W., & Teriaca, L. 2023, *JApA*, **44**, 20
- Mishra, W., & Wang, Y. 2018, *ApJ*, **865**, 50
- Mishra, W., Wang, Y., Lyu, S., & Khuntia, S. 2023, *ApJ*, **952**, 173
- Mishra, W., Wang, Y., Srivastava, N., & Shen, C. 2017, *ApJS*, **232**, 5
- Mishra, W., Wang, Y., Teriaca, L., Zhang, J., & Chi, Y. 2020, *FrASS*, **7**, 1
- Möstl, C., Farrugia, C. J., Kilpua, E. K. J., et al. 2012, *ApJ*, **758**, 10
- Möstl, C., Weiss, A. J., Reiss, M. A., et al. 2022, *ApJL*, **924**, L6
- Nieves-Chinchilla, T., Jian, L. K., Balmaceda, L., et al. 2019, *SoPh*, **294**, 89
- Nieves-Chinchilla, T., Vourlidas, A., Stenborg, G., et al. 2013, *ApJ*, **779**, 55
- Ogilvie, K. W., & Desch, M. D. 1997, *AdSpR*, **20**, 559
- Owens, M. J., Lockwood, M., & Barnard, L. A. 2017, *NatSR*, **7**, 4152
- Palmerio, E., Kilpua, E. K. J., Möstl, C., et al. 2018, *SpWea*, **16**, 442
- Pulkkinen, T. 2007, *LRSP*, **4**, 1
- Regnault, F., Al-Haddad, N., Lugaz, N., et al. 2023, *ApJ*, **957**, 49
- Regnault, F., Al-Haddad, N., Lugaz, N., et al. 2024, *ApJ*, **962**, 190
- Richardson, I. G., & Cane, H. V. 2010, *SoPh*, **264**, 189
- Rosa Oliveira, R. A., da Silva Oliveira, M. W., Ojeda-González, A., et al. 2021, *SoPh*, **296**, 182
- Salman, T. M., Winslow, R. M., & Lugaz, N. 2020, *JGRA*, **125**, e27084
- Schrijver, C. J., Kauristie, K., Aylward, A. D., et al. 2015, *AdSpR*, **55**, 2745
- Schwenn, R. 2006, *LRSP*, **3**, 2
- Sheeley, N. R., Walters, J. H., Wang, Y. M., & Howard, R. A. 1999, *JGR*, **104**, 24739
- Siscoe, G. L., & Suey, R. W. 1972, *JGR*, **77**, 1321
- Song, H. Q., Zhang, J., Cheng, X., et al. 2020, *ApJL*, **901**, L21
- Sonnerup, B. U. Ö., & Cahill, L. J. J. 1967, *JGR*, **72**, 171
- Sonnerup, B. U. Ö., & Scheible, M. 1998, *ISSIR*, **1**, 185
- Srivastava, N., & Venkatakrishnan, P. 2004, *JGRA*, **109**, A10103
- Temmer, M., Scolini, C., Richardson, I. G., et al. 2023, arXiv:2308.04851
- Temmer, M., Veronig, A. M., Peinhart, V., & Vršnak, B. 2014, *ApJ*, **785**, 85
- Thernisien, A. F. R., Howard, R. A., & Vourlidas, A. 2006, *ApJ*, **652**, 763
- Wang, C., Du, D., & Richardson, J. D. 2005, *JGRA*, **110**, A10107
- Wang, Y., Shen, C. L., Wang, S., & Ye, P. Z. 2003, *GeoRL*, **30**, 2039
- Webb, D. F., & Howard, T. A. 2012, *LRSP*, **9**, 3
- Winslow, R. M., Lugaz, N., Philpott, L. C., et al. 2015, *JGRA*, **120**, 6101
- Winslow, R. M., Lugaz, N., Schwadron, N. A., et al. 2016, *JGRA*, **121**, 6092
- Winslow, R. M., Lugaz, N., Scolini, C., & Galvin, A. B. 2021, *ApJ*, **916**, 94
- Wood, B. E., Wu, C.-C., Lepping, R. P., et al. 2017, *ApJS*, **229**, 29
- Xie, H., Ofman, L., & Lawrence, G. 2004, *JGRA*, **109**, A03109
- Zhang, J., Hess, P., & Poomvises, W. 2013, *SoPh*, **284**, 89
- Zurbuchen, T. H., & Richardson, I. G. 2006, *SSRv*, **123**, 31